Resolution Analysis in a Lens-Free On-Chip Digital Holographic Microscope

Jialin Zhang, Jiasong Sun, Qian Chen, and Chao Zuo, *Member, IEEE*

***Abstract*—Lens-free on-chip digital holographic microscopy (LFOCDHM) is a modern imaging technique whereby the sample is placed directly onto or very close to the digital sensor, and illuminated by a partially coherent source located far above it. The scattered object wave interferes with the reference (unscattered) wave at the plane where a digital sensor is situated, producing a digital hologram that can be processed in several ways to extract and numerically reconstruct an in-focus image using the back propagation algorithm. Without requiring any lenses and other intermediate optical components, the LFOCDHM has unique advantages of offering a large effective numerical aperture (NA) close to unity across the native wide field-of-view (FOV) of the imaging sensor in a cost-effective and compact design. However, unlike conventional coherent diffraction limited imaging systems, where the limiting aperture is used to define the system performance, typical lens-free microscopes only produce compromised imaging resolution that far below the ideal coherent diffraction limit. At least five major factors may contribute to this limitation, namely, the sample-to-sensor distance, spatial and temporal coherence of the illumination, finite size of the equally spaced sensor pixels, and finite extent of the image sub-FOV used for the reconstruction, which have not been systematically and rigorously explored until now. In this article, we derive five transfer function models that account for all these physical effects and interactions of these models on the imaging resolution of LFOCDHM. We also examine how our theoretical models can be utilized to optimize the optical design or predict the theoretical resolution limit of a given LFOCDHM system. We present a series of simulations and experiments to confirm the validity of our theoretical models.**

***Index Terms*—Lens-free microscopy, digital holography (LFOCDHM), resolution analysis.**

I. Introduction

HIGH-THROUGHPUT optical microscopy is essential to various biomedical applications such as cell cycle assay, drug development, digital pathology, and high-content biological screening [1], [2]. For conventional whole slide imaging (WSI) systems, in order to capture a high-throughput image with both high-resolution and large field of view (FOV), mechanical scanning and stitching are required to expand the limited FOV of a conventional high magnification objective [3], which not only complicate the imaging process, but also significantly increase the overall cost of the system. The recently developed computational microscopy techniques provide new opportunities to create high-resolution wide FOV images without any mechanical scanning and stitching, such as synthetic aperture interferometric microscopy [4]–[9], Fourier ptychography microscopy (FPM) [10]–[16], and lens-free on-chip microscopy [17]–[20]. Among these approaches, the lens-free on-chip microscopy has unique advantages of achieving a large effective numerical aperture (NA) ~ 1 across the native FOV of the imaging sensor (tens of mm^2), based on a so-called unit-magnification configuration, where the samples are placed as close as possible to the imaging sensor [21], [22]. Without requiring any lenses and other optical components between the object and the sensor planes, lens-free on-chip microscopy allows to significantly simplify the imaging system and meanwhile effectively circumvent the optical aberrations and chromaticity that are inevitable in conventional lens-based imaging systems [23], [24]. There are two typical designs for a lens-free on-chip microscope, so-called contact-mode shadow imaging-based microscope [17], [25] and lens-free on-chip digital holographic microscope (LFOCDHM) [21], [26]. In the contact-mode shadow imaging-based microscopes, the distance between the sample and the sensor needs to be quite small (typically less than 10 μm), and the captured shadows of the objects can be regarded as a two-dimensional absorption image of the specimen [27]. However, the small distance is very difficult to achieve in practice due to the existence of protective glass covering the surface of the camera sensor. In LFOCDHM, the distance between the objects and the sensor chip can be sizeable, and diffraction patterns are generated from the interference between the scattered light from each object

Manuscript received June 20, 2019; revised October 30, 2019; accepted December 16, 2019. Date of publication January 6, 2020; date of current version February 6, 2020. This work was supported in part by the National Natural Science Foundation of China under Grants 61722506 in part by the Leading Technology of Jiangsu Basic Research Plan BK20192003, in part by the Final Assembly "13th Five-Year Plan" Advanced Research Project of China under Grant 30102070102, in part by the Equipment Advanced Research Fund of China under Grant 61404150202, in part by the National Defense Science and Technology Foundation of China under Grant 0106173, in part by the Outstanding Youth Foundation of Jiangsu Province under Grant BK20170034, in part by The Key Research and Development Program of Jiangsu Province under Grant BE2017162, in part by the "333 Engineering" Research Project of Jiangsu Province under Grant BRA2016407, and in part by the Fundamental Research Funds for the Central Universities under Grant 30917011204, and in part by the Open Research Fund of Jiangsu Key Laboratory of Spectral Imaging & Intelligent Sense (3091801410411). The associate editor coordinating the review of this manuscript and approving it for publication was Prof. G. Wetzstein. *(Corresponding author: Chao Zuo.)*

Jialin Zhang, Jiasong Sun, and Chao Zuo are with the School of Electronic and Optical Engineering, Nanjing University of Science and Technology, Nanjing, Jiangsu Province 210094, China, and with the Jiangsu Key Laboratory of Spectral Imaging & Intelligent Sense, Nanjing, Jiangsu Province 210094, China, and also with the Smart Computational Imaging Laboratory (SCILab), Nanjing University of Science and Technology, Nanjing, Jiangsu Province 210094, China (e-mail: JialinZhang@njust.edu.cn; sunjiasong@njust.edu.cn; zuochao@njust.edu.cn).

Qian Chen is with the School of Electronic and Optical Engineering, Nanjing University of Science and Technology, Nanjing, Jiangsu Province 210094, China, and also with the Jiangsu Key Laboratory of Spectral Imaging & Intelligent Sense, Nanjing, Jiangsu Province 210094, China (e-mail: chenqian@njust.edu.cn).

Digital Object Identifier 10.1109/TCI.2020.2964247

and itself or the unscattered background light. The diffraction patterns are digitally processed to reconstruct an image of the specimen, and the associated twin-image artifacts need to be eliminated or partially removed relying on computational phase retrieval algorithms [28], [29]. In the following analysis, we will examine LFOCDHM exclusively.

Despite the advantages mentioned earlier, the LFOCDHM systems generally suffer from low imaging resolution which is far from enough to meet the demand of recent biomedical research, particularly with respect to the visualization of cellular or subcellular details of biological structures and processes. Unlike conventional coherent diffraction limited imaging systems, where the limiting aperture is used to define the system performance, typical LFOCDHM systems only produce compromised imaging resolution that far below the ideal coherent diffraction limit. According to Nyquist-Shannon sampling theorem, the resolution of the holographic reconstruction is fundamentally limited to the sampling resolution of the imaging devices since the recorded holographic fringes are not magnified. In other words, the physical pixel size is one important limiting factor of these lens-free imaging systems [27]. Because of the spatial aliasing/undersampling, the imaging sensor will fail to record holographic oscillation corresponding to high spatial frequency information of the specimen. To address this problem, pixel super-resolution (SR) methods have been proposed in which the hologram with a smaller effective pixel size can be synthesized from multiple low-resolution (LR) measurements through specific computational algorithms [17], [18], [25], [26], [30]. With these pixel SR methods, the imaging resolution of the LFOCDHM systems can be improved from Nyquist-Shannon limit (half-pitch lateral resolution of $\sim 2\ \mu$m, effective NA of $\sim 0.1 - 0.2$) to an effective numerical aperture of $\sim 0.4 - 0.5$ [17], [18], [26], [31].

However, the achieved imaging resolution is still only less than half of the ideal coherent diffraction limit (NA ~ 1). The reason for this is that besides the pixel size of the sensor, other features, e.g., the pixel averaging effect within the finite detection size of one pixel (the fill factor), may also result in the LR reconstructions [32]. Although all these characteristics of sensors may lead to the unsatisfactory reconstruction resolution, in the current common LFOCDHM systems, the incident angle of the illumination light has not exceeded the limit of the camera, and the pixel size is attributed to the main factor in the characteristics of the sensor [27]. Besides the pixel size, at least four additional factors act to significantly limit the performance of LFOCDHM systems, namely, the sample-to-sensor distance, spatial and temporal coherence of the illumination, and finite extent of the image sub-FOV used for the reconstruction. This is not unexpected and has been discussed by other authors, for example, Refs. [18], [27]. However, either only qualitative analyses were presented [33], [34], or only one or two of these factors on the imaging resolution have been considered [32], [34]–[36]. In these quantitative analyses [32], [35], [36], the discrete features of the sensor attracts more attention, but the other basic parameters of the LFOCDHM systems, e.g., the sample-to-sensor distance [37], spatial and temporal coherence of the illumination [34], and finite extent of the image sub-FOV [38], are sporadically mentioned in the off-axis/in-line digital holographic microscopy. The influence of these five factors on the imaging resolution of LFOCDHM has not been systematically examined and rigorously explored until now.

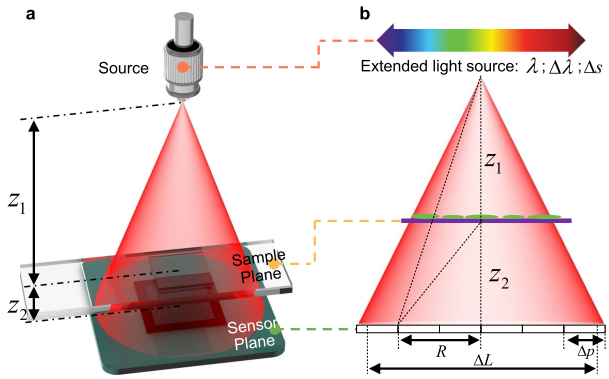

Fig. 1. (a) General lens-free imaging experimental setup. (b) Schematic of a lens-free holographic microscope. The sample is illuminated with wavelength λ, the spectral width $\Delta\lambda$, the diameter of the light-emitting area Δs. The diffraction patterns are registered by a sensor with pitch Δp at a distance z_2.

In this work, we conduct a systematical research on the effect of five major factors on imaging resolution of a LFOCDHM system, i.e., the sample-to-sensor distance, spatial and temporal coherence of the illumination, finite size of the equally spaced sensor pixels, and finite extent of the image sub-FOV used for the reconstruction. We derive five transfer function models that account for all these physical effects and their interactions on the imaging resolution of LFOCDHM. We further combine all these effects into a unified transfer function, which is the continued multiplication of the five sub-transfer functions. We examine how these theoretical models can be utilized to predict the theoretical resolution limit of a given LFOCDHM system or provide a useful guide to the selection of different system parameters for the optimization of the imaging resolution when designing a new LFOCDHM system. A series of simulations and experiments are presented to confirm the validity of our theoretical models. In order to avoid the influence of multi-height selection on the reconstruction quality, in the following part of this work, all simulations and experiments will be carried out with single-height measurement.

II. Principle

A. Typical Optical Setup for LFOCDHM

In the lens-free holographic microscope as depicted in Fig. 1(a), the source can simply be a laser [20], [39], [40], a LED (an array of LEDs) [41]–[44] or even a smartphone screen [17]. The coherent or partially coherent light illuminates the specimen, and then the scattered light and the transmitted light co-propagate in the same direction, finally forming interference fringes on the imaging device. In the ideal case, the sample should be placed on a sensor array which can directly capture the shadows of the objects and avoid the twin-image artifacts.

However, due to the existence of protective glass covering the surface of the camera sensor, there is usually always a certain distance between the sample plane and the detector plane (typically $0.3-2$ mm) [22], [26], [45]. The distance is much larger than the wavelength, and thus the object information (including both amplitude and phase) is encoded into the diffraction patterns, which needs to be computationally reconstructed by phase retrieval and numerical back propagation algorithms.

As illustrated in the schematic diagram Fig. 1(b) of the lens-free holographic microscope, neglecting the noise effect, the achievable resolution of LFOCDHM is determined by the maximum visualized radius R of the diffraction patterns, which refer to the cut-off frequency of the transfer function. This transfer function can be further decomposed into five sub-transfer functions, and the least cut-off frequency of the five transfer functions limits the maximum imaging resolution of LFOCDHM. The five sub-transfer functions respectively correspond to the impact of the defocus distance z_2, the temporal coherence (the spectral width $\Delta\lambda$), the spatial coherence (the diameter of light-emitting area Δs) of the source, the finite pixel size (Δp), and the finite extent of the image sub-FOV used for the reconstruction (the side length ΔL). The absorption and phase transfer functions resulting from propagation are respectively denoted as $ATFP$ and $PTFP$. Then the temporal coherence transfer function, the spatial coherence transfer function, pixel size transfer function, the reconstructed region transfer function are severally expressed as $TCTF$, $SCTF$, $PSTF$, $RRTF$. Here, the latter four sub-transfer functions are mutually independent, and together have impacts on the final imaging results.

B. Theoretical Analysis of Resolution in LFOCDHM

1) Influence of Sample-to-Sensor Distance on Imaging Resolution: In this subsection, we adopt the weak object approximation to simplify the mathematical formulation and linearize the phase retrieval problem [46], [47]. Before reaching the digital camera, the object complex wave-front is propagated over the distance of z_2 in air (the medium of refractive index ≈ 1) with the angular spectrum method [48], and thus the spectrum of the complex wave-front on the camera plane $W_{cam}(\mathbf{u})$ is equivalent to introducing an imaginary part into the transmitted complex wave-front in the Fourier domain (see details in Appendix A). In the frequency space, the intensity spectrum can be obtained by calculating the autocorrelation of $W_{cam}(\mathbf{u})$ [48]:

$$\begin{aligned}\tilde{I}_{cam}(\mathbf{u}) &= W_{cam}(\mathbf{u}) * W'_{cam}(-\mathbf{u}) \\ &\approx a_0^2 P'(0)P(0) + a_0 A(\mathbf{u})\left[P'(0)P(\mathbf{u}) + P(0)P'(\mathbf{u})\right] \\ &\quad + i a_0^2 \Phi(\mathbf{u})\left[P'(0)P(\mathbf{u}) - P(0)P'(\mathbf{u})\right], \end{aligned} \tag{1}$$

where $\mathbf{u}$ is the two-dimensional coordinate in frequency domain, $*$ denotes the convolution, $'$ represents the complex conjugation, $\delta(\mathbf{u})$ is the Dirac Delta function, $A(\mathbf{u})$ and $\Phi(\mathbf{u})$ respectively represent the Fourier spectrum of the absorption and phase distribution, $P(\mathbf{u})$ represents the defocus pupil function. In Eq. (1), we have neglected the high order convolution terms between $A(\mathbf{u})$ and $\Phi(\mathbf{u})$ [49]. Thus, the absorption transfer function ($ATFP$) and phase transfer function ($PTFP$) of LFOCDHM with the defocus distance z_2 can be written as:

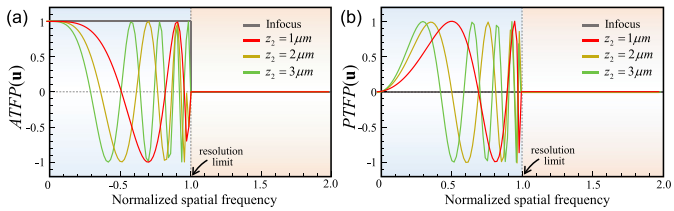

Fig. 2. The absorption transfer function $ATFP(\mathbf{u})$ (a) and phase transfer function $PTFP(\mathbf{u})$ (b) for various defocus distances. $\lambda = 600$ nm, the spatial frequency coordinate is normalized against the resolution limit $1/\lambda$.

$$\begin{aligned} ATFP &= a_0\left[P'(0)P(\mathbf{u}) + P(0)P'(\mathbf{u})\right] \\ &= 2a_0 \cos\left[kz_2\left(1-\sqrt{1-\lambda^2|\mathbf{u}|^2}\right)\right], \end{aligned} \tag{2}$$

$$\begin{aligned} PTFP &= a_0^2\left[P'(0)P(\mathbf{u}) - P(0)P'(\mathbf{u})\right] \\ &= -2a_0^2 \sin\left[kz_2\left(1-\sqrt{1-\lambda^2|\mathbf{u}|^2}\right)\right]. \end{aligned} \tag{3}$$

The transfer functions of $ATFP(\mathbf{u})$ and $PTFP(\mathbf{u})$ with the wavelength 600 nm are shown in Fig. 2 for various defocus distances and the response value of them has been normalized to $0-1$. The sample-to-sensor distance z_2 varies from 1 μm to 3 μm. Fig. 2(a) shows that with the increase in defocus distance, $ATFP(\mathbf{u})$ decreases earlier and the declining rate of these curves accelerates. Moreover, the increase in defocus distance also introduces higher oscillation frequency with more zero-crossings. The low responses of frequency around these zero-crossing points pose severe difficulties for the information reconstruction at these corresponding frequencies, suggesting that the information at these frequencies can no longer transfer into intensity and such high oscillation should be avoided as much as possible. Thus, for $ATFP(\mathbf{u})$, the smaller defocus distance will benefit for the reconstructed intensity image. However, for phase imaging $PTFP(\mathbf{u})$, Fig. 2(b) shows that the response of frequency around the origin is always very low, suggesting the low-frequency phase can hardly transfer into intensity via defocusing. As the defocus distance getting large, the response at low frequencies gradually increases. In other words, large defocus distance is conducive to the recovery of the low-frequency phase information. Nevertheless, the accompanied high oscillation frequency will also introduce a large number of zero-crossing points.

Thus, for the reconstruction of phase objects based on single sample-to-sensor distance, the selection of the defocus distance faces a fundamental tradeoff between low-frequency information reconstruction quality and the loss of frequency components. In general, multiple sample-to-sensor distances are required to construct a synthetic phase transfer function with high responses over a wider range of spatial frequencies:

$$ATFP_{syn}(\mathbf{u}) = \frac{1}{N_{total}} \sum_{i=1}^{N_{total}} \left| ATFP\left(z_2^i, \mathbf{u}\right)\right|$$

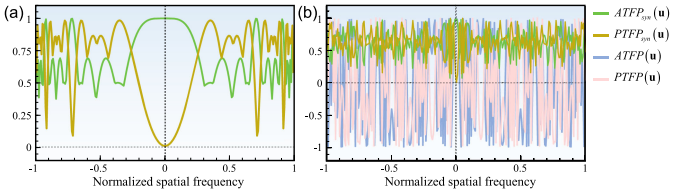

Fig. 3. (a) The synthesized absorption transfer function $ATFP_{syn}(\mathbf{u})$ and synthesized phase transfer function $PTFP_{syn}(\mathbf{u})$ with various defocusing distances ($z_2 = 1, 2, 3$ μm); (b) The absorption transfer function $ATFP(\mathbf{u})$ and phase transfer function $PTFP(\mathbf{u})$ with $z_2 = 400$ μm; $ATFP_{syn}(\mathbf{u})$ and $PTFP_{syn}(\mathbf{u})$ with various defocusing distances ($z_2 = 400$, 410, 420 μm).

$$PTFP_{syn}\left(\mathbf{u}\right) = \frac{1}{N_{total}} \sum_{i=1}^{N_{total}} \left|PTFP\left(z_2^i, \mathbf{u}\right)\right|, \quad (4)$$

where z_2^i represents the different defocus distances and N_{total} is the total number of defocus planes. Under the same simulation conditions, the synthesized transfer functions of $ATFP_{syn}(\mathbf{u})$ and $PTFP_{syn}(\mathbf{u})$ are shown in Fig. 3(a). Fig. 3(a) shows that the multi-height measurements can significantly reduce the number of zero-crossings by synthesization of transfer function. However, the recovery of the very low frequency (near zero frequency) phase component is still quite difficult. In the practical experiment, due to the cover glass of the sensor, the defocusing distance usually exceeds 400 μm, and the oscillation frequency of $ATFP(\mathbf{u})$ and $PTFP(\mathbf{u})$ is extremely high, as shown in Fig. 3(b). Fortunately, such a large distance can effectively reduce the low-response frequencies range, which is beneficial to recover the frequency components near zero-crossing points.

Generally, when the components of the lens-free imaging system such as the light source and the sensor have been predetermined, multi-height measurements can optimize the synthetic transfer functions, which is beneficial for the intensity and phase reconstruction quality. But for single-height measurement, limited by the relatively large defocusing distance, the influence of defocusing distance on the reconstruction result can be neglected due to the rapid oscillation of the transfer functions.

2) Influence of Temporal Coherence on Imaging Resolution: In this subsection, we will analyze the influence of temporal coherence on imaging resolution, which can be attributed to the temporal coherence transfer function ($TCTF$). It is assumed that the temporal coherence is the only factor affecting the reconstruction resolution. Suppose that the central wavelength λ, the spectrum width $\Delta\lambda$, the spectral distribution $S_\lambda(\lambda_i)$ are the predetermined parameters, and other system parameters are close to ideal values (do not affect the imaging resolution). If we further invoke the paraxial approximations [47], the two transfer functions Eqs. (2) and (3) can be simplified as $ATFP \approx 2a_0 \cos(\pi z_2 \lambda |\mathbf{u}|^2)$, $PTFP \approx -2a_0^2 \sin(\pi z_2 \lambda |\mathbf{u}|^2)$. If the effect of spectral width of the illumination source is further taken into account, the absorption and phase transfer functions of LFOCDHM with the sample-to-sensor distance z_2 and the actual wavelength λ_i can be represented as:

$$ATF_{p+t}\left(\mathbf{u}\right) = 2a_0 \int S_\lambda\left(\lambda_i\right) \cos\left(\pi z_2 \lambda_i |\mathbf{u}|^2\right) d\lambda_i$$

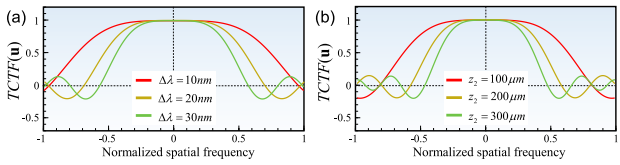

Fig. 4. The temporal coherence transfer function $TCTF(\mathbf{u})$. (a) $TCTF(\mathbf{u})$ for various spectral width $\Delta\lambda$ with the defocusing distance $z_2 = 200$ μm. (b) $TCTF(\mathbf{u})$ for various defocusing distances with the spectral width $\Delta\lambda = 30$ nm.

$$PTF_{p+t}\left(\mathbf{u}\right) = -2a_0^2 \int S_\lambda\left(\lambda_i\right) \sin\left(\pi z_2 \lambda_i |\mathbf{u}|^2\right) d\lambda_i. \quad (5)$$

In most cases, the spectral distribution S_λ can be approximated by a Gaussian function:

$$S_\lambda\left(\lambda_i\right) = e^{-\frac{\left(\lambda_i - \lambda\right)^2}{0.36\Delta\lambda^2}}, \quad (6)$$

where λ can be noted as the mean value and the standard deviation is $0.424\Delta\lambda$. Here standard deviation $0.424\Delta\lambda$ is assumed to ensure that the normalized intensity of the wavelengths varying in the range of $[\lambda - \Delta\lambda/2, \lambda + \Delta\lambda/2]$ is not less than half maximum intensity. By incorporating the effect of temporal coherence, the transfer functions can be further expressed as the integrals over the full spectral range:

$$\begin{aligned} ATF_{p+t}\left(\mathbf{u}\right) &= 2a_0 \int_{-\Delta\lambda/2+\lambda}^{\Delta\lambda/2+\lambda} e^{-\frac{\left(\lambda_i - \lambda\right)^2}{0.36\Delta\lambda^2}} \cos\left(\pi z_2 \lambda_i |\mathbf{u}|^2\right) d\lambda_i \\ PTF_{p+t}\left(\mathbf{u}\right) &= -2a_0^2 \int_{-\Delta\lambda/2+\lambda}^{\Delta\lambda/2+\lambda} e^{-\frac{\left(\lambda_i - \lambda\right)^2}{0.36\Delta\lambda^2}} \sin\left(\pi z_2 \lambda_i |\mathbf{u}|^2\right) d\lambda_i. \end{aligned} \quad (7)$$

Although Eq. (7) is an integrable function in real space theoretically, the result cannot provide a well-defined analytical cut-off frequency expression. To give the theoretical cut-off frequency limit, in consideration of the ideal spectral distribution, we assume that $S_\lambda(\lambda_i)$ is a rectangular function, and then ATF_{p+t} and PTF_{p+t} will be noted as:

$$\begin{aligned} ATF_{p+t}\left(\mathbf{u}\right) &= ATFP\left(\mathbf{u}\right) sinc\left(z_2 \frac{\Delta\lambda}{2} |\mathbf{u}|^2\right) \\ PTF_{p+t}\left(\mathbf{u}\right) &= PTFP\left(\mathbf{u}\right) sinc\left(z_2 \frac{\Delta\lambda}{2} |\mathbf{u}|^2\right). \end{aligned} \quad (8)$$

Therefore, the finite spectral width is equivalent to introducing an additional $sinc$ term into the transfer functions. Since the temporal coherence of the LFOCDHM system plays equally important role in the $ATFP(\mathbf{u})$ and $PTFP(\mathbf{u})$, we use $TCTF(\mathbf{u})$ to represent the overall influence of finite spectral width:

$$TCTF\left(\mathbf{u}\right) = sinc\left(z_2 \frac{\Delta\lambda}{2} |\mathbf{u}|^2\right). \quad (9)$$

Then the temporal coherence transfer functions $TCTF(\mathbf{u})$ for different spectral width $\Delta\lambda$ and various defocus distances are shown in Fig. 4. In Fig. 4(a), under the condition of $z_2 = 200$ μm, $\lambda = 660$ nm, the spectral width $\Delta\lambda$ varying from 10 nm to 30 nm, as $\Delta\lambda$ gets wider, the frequency response decreases more rapidly and reaches zero earlier (at so-called the first

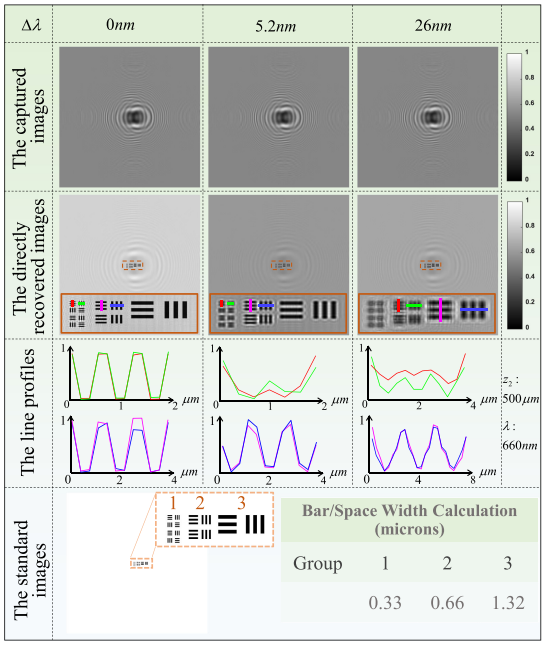

Fig. 5. The quantitative reconstruction results varying in the different spectral width $\Delta\lambda$. The simulation condition: $z_2 = 500$ μm, $\lambda = 660$ nm, $\Delta\lambda = 0, 5.2, 26$ nm. The first row: the raw images; The second row: the directly reconstructed images with the angular spectrum method; The third row: the line profiles corresponding to the marks on the image in the second row; The fourth row: the standard resolution target for the simulation.

zero-crossing or the first cut-off frequency). The response of the frequencies above the first cut-off frequency may slightly overshoot, but these frequency components are difficult to be recovered since the response is highly fluctuant. In contrast, for a given defocusing distance z_2, higher temporal coherence of the light source (decreasing $\Delta\lambda$) provides a wider range of the high-response frequency regions and higher cut-off frequency, which is beneficial to improve the imaging resolution. In actual experiments, $\Delta\lambda$ usually is pre-defined parameter while the defocus distance z_2 is flexible, and thus the frequency response curves will be similar to those shown in Fig. 4(b). The first cut-off frequency will gradually increase as the defocusing distance decreases when the parameters of the light source are fixed. From Eq. (9), we can deduce that the first cut-off frequency is $|\mathbf{u}| = \sqrt{\frac{2}{z_2\Delta\lambda}}$, and the corresponding reconstructed half-pitch resolution is

$$q = \frac{1}{2\,|\mathbf{u}|} = \sqrt{\frac{z_2\Delta\lambda}{8}}. \tag{10}$$

To verify the resolution limit resulting from the finite spectral width $\Delta\lambda$, we simulate a resolution target under conditions of $z_2 = 500$ μm, $\lambda = 660$ nm, as shown in Fig. 5. From the line profiles in Fig. 5, we can see that each element of the resolution target can be recovered when the light source is perfectly coherent, but the high-frequency elements gradually become blurred with the increase of $\Delta\lambda$. More specifically, when $\Delta\lambda$ is 5.2 nm, the theoretical half-pitch resolution is $q = 0.57$ μm, which coincides well with the simulation result shown in Fig. 5. For $\Delta\lambda = 26$ nm, the elements of group 3 can be distinguished easily, but elements of group 2 are barely discernable. According to Eq. (10) (the theoretical resolution $q = 1.27$ μm), group 2 of the target should be completely indistinguishable, so the slightly discernible elements may result from the non-zero responses of the transfer function beyond the first cut-off frequency, as shown in Fig. 4.

In summary, the temporal coherence has an impact on the ultimate imaging resolution of the LFOCDHM system. Increasing temporal coherence of the source by using a laser, or inserting a narrow band-pass filter in front of the source can directly reduce its influence on the resolution. When the light source of the system is determined ($\Delta\lambda$ is a constant value), it should be guaranteed that the object-to-sample distance z_2 must be smaller than $2\lambda^2/\Delta\lambda$ (guarantee q is smaller than $\lambda/2$) so that the temporal coherence of the source does not influence the final resolution, and the reconstructed resolution will be only affected by the ideal coherent diffraction limit ($\lambda/2$). For example, when the spectrum width of illumination source is about 20 nm and the ideal half-pitch resolution limit is 0.3 μm, the object-to-sample distance z_2 should be smaller than 36 μm ideally. However, for imaging phase objects, z_2 should not be too small to guarantee sufficient responses of the phase transfer function, which is crucial to the recovery accuracy of low-frequency phase information. As mentioned earlier, due to the manufacturing technology of commercial sensors, the defocusing distance z_2 is difficult to go below 300 μm. When the distance z_2 cannot be small enough, we should use a light source with higher temporal coherence (narrower spectral width $\Delta\lambda$) to guarantee the diffraction-limited imaging resolution.

3) Influence of Spatial Coherence on Imaging Resolution: In this subsection, we will analyze the influence of spatial coherence on imaging resolution, which can be attributed to the spatial coherence transfer function ($SCTF$). In addition to the temporal coherence, the spatial coherence also affects the reconstructed resolution. Same as before, we assume that the reconstructed resolution is only affected by the spatial coherence of the light source, and the sample is illuminated by the light emitting from a spatially incoherent delta-correlated light source (any two different points in the source plane are uncorrelated). Thus, the captured image influenced by the finite spatial coherence $I_{cap}(\mathbf{x})$ can be modeled as a convolution of the ideal in-line hologram $I(\mathbf{x})$ (arising from the central point source) with a properly resized source intensity distribution S_s [50], [51].

$$I_{cap}(\mathbf{x}) = I(\mathbf{x}) * \left[\left(\frac{z_1}{z_2}\right)^2 \times S_s\left(\frac{z_1}{z_2}\mathbf{x}\right)\right] = I(\mathbf{x}) * PSF(\mathbf{x}), \tag{11}$$

where $\mathbf{x}$ represents the coordinates in the imaging sensor plane. Without loss of generality, the scaled factor $(z_1/z_2)^2$ can be neglected. According to Eq. (11), assuming that the illumination source is circular with a diameter of Δs, $SCTF$ can be expressed as (see details in Appendix B when the shape of the source is a rectangle):

$$SCTF(\mathbf{u}) = \mathcal{F}(PSF) = \frac{J_1\left(2\pi\frac{z_2\Delta s}{2z_1}|\mathbf{u}|\right)}{|\mathbf{u}|}, \tag{12}$$

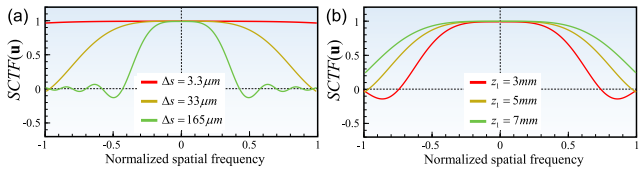

Fig. 6. The spatial coherence transfer function $SCTF(\mathbf{u})$. (a) $SCTF(\mathbf{u})$ for different Δs. ($z_1 = 5$ mm, $z_2 = 200$ μm) (b) $SCTF(\mathbf{u})$ for various defocus distances with the diameter of the light-emitting zone $\Delta s = 33$ μm. ($z_2 = 200$ μm)

where J_1 represents the Bessel function of the first kind. The simulation results of the transfer function $SCTF(\mathbf{u})$ for different source sizes and defocus distances are shown in Fig. 6. In Fig. 6(a), $\Delta\lambda \to 0$, $\lambda = 660$ nm, $z_1 = 5$ mm, $z_2 = 200$ μm, $\Delta s = 3.3, 33, 165$ μm are given to analyze the resolution limit resulting from the spatial coherence. From the simulation results of Fig. 6(a), the effect of the spatial coherence on the reconstruction resolution will reduce as Δs getting smaller. From the curves of $SCTF(\mathbf{u})$ in Fig. 6(a), while Δs gets larger, the response of the transfer function decreases earlier and reaches the first cut-off frequency more rapidly.

In actual experiments, when the illumination source is determined, the diameter of the luminous area (Δs) is unalterable. Under such condition, in order to improve the spatial coherence, we can increase the shrink ratio of z_1/z_2 to reduce the effective illumination area, alternatively. In our simulations, the system parameters are $\Delta\lambda \to 0$, $\lambda = 660$ nm, $z_1 = 3, 5, 7$ mm, $z_2 = 200$ μm, $\Delta s = 33$ μm, and the frequency response curves are shown in Fig. 6(b). From these curves, we can observe that larger z_1/z_2 will increase the first cut-off frequency, and thus, improve the reconstruction resolution.

Based on Eq. (12), we can derive that the first cut-off frequency is $|\mathbf{u}| = \frac{3.8}{\pi} \cdot \frac{z_1}{z_2 \Delta s}$, where the constant 3.8 is determined by the zeros of the Bessel function, and the corresponding reconstructed half-pitch resolution is

$$q = \frac{1}{2\,|\mathbf{u}|} = \frac{\pi}{7.6} \cdot \frac{z_2 \Delta s}{z_1}. \tag{13}$$

This reconstruction resolution involves many parameters and factors according to Eq. (13). In Fig. 7, $z_1 = 30$ mm, $z_2 = 500$ μm are given to verify the resolution limit. In Fig. 7, when Δs gradually increases, the reconstruction resolution will get worse correspondingly. For example, when $\Delta s = 68$ μm, the theoretical resolution is 0.46 μm, and the corresponding simulation result is 0.66 μm which is lower than that of the ideal illumination $\Delta s \to 0$. If Δs further increases to 153 μm, the resolution reduces to 1.32 μm, which agrees with the theoretical value 1.05 μm.

From the above analysis, we know that the spatial coherence may affect the ultimate imaging resolution of the LFOCDHM system, which is associated with the ratio z_2/z_1 and Δs. Thus, in the lens-free experimental setups, when the LED is used as a light source, there are several ways to improve the spatial coherence and reduce its effect on imaging resolution. On the one hand, we can insert a small pin-hole in front of the source to reduce the source size. On the other hand, we can reduce to ratio z_2/z_1 to reduce the effective size of the source. As we mentioned

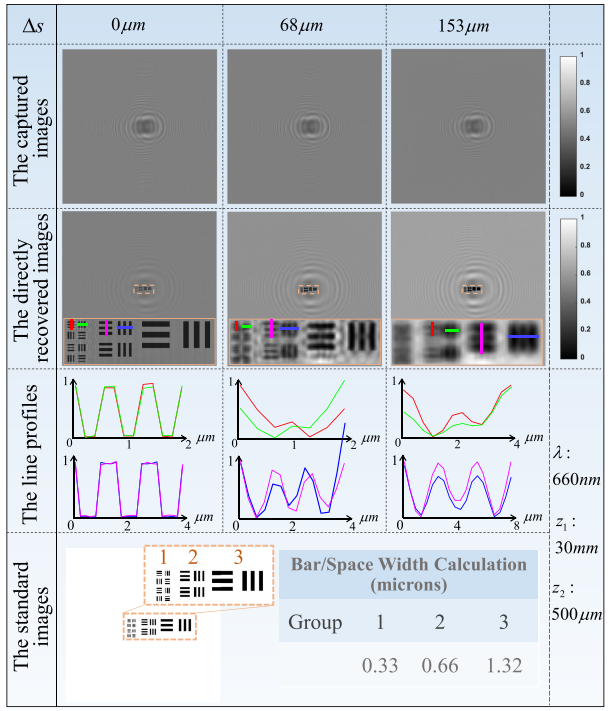

Fig. 7. The quantitative reconstruction results varying in the diameters of illumination source Δs. The simulation condition: $z_1 = 30$ mm, $z_2 = 500$ μm, $\lambda = 660$ nm, $\Delta s = 0, 68, 153$ μm. The first row: the raw images; The second row: the directly reconstructed images with the angular spectrum method; The third row: the line profiles corresponding to the marks on the image in the second row; The fourth row: the standard resolution target for the simulation.

earlier, the object-to-sample distance z_2 cannot be too small, so we can increase the source-to-sample distance z_1 instead. All these experimental manipulations are utilized to avoid the effect of the poor spatial coherence on the reconstruction resolution, and guarantee that the diffraction-limited imaging resolution q (Eq. (13) or Eq. (24)) is smaller than $\lambda/2$. For example, when the diameter Δs of illumination source is about 200 μm and the ideal half-pitch resolution limit is 0.3 μm, ratio z_2/z_1 must be smaller than 0.0036 theoretically. However, for actual imaging objects, z_2 is usually larger than 300 μm, and thus, to guarantee sufficient responses of the transfer function, z_1 must be larger than 83.33 mm. Consequently, for an established lens-free microscopic imaging system, the effect of spatial coherence can be avoided as far as possible by increasing z_1, and the minimum value of z_1 can also be obtained by Eq. (13).

4) Influence of Sensor Pixel Size on Imaging Resolution: In lens-free imaging system, the pixel size is a key factor influencing the achievable spatial resolution. We assume that the finest feature to be captured corresponds to the half-pitch resolution $\Delta p/w$, where $w \geqslant 1$ and the number of pixels of this image is $M \times N$. Then suppose the actual pixel size of the camera is Δp with $m \times n$ pixels. The ideal pixel aliasing can be interpreted as a procedure that the ideal image is first pixel binned and then sub-sampled. Specifically, the pixel binning effect can be modeled as convolution process with the convolution kernel S_a:

$$I_{bin}(\mathbf{x}) = I(\mathbf{x}) * S_a, \tag{14}$$

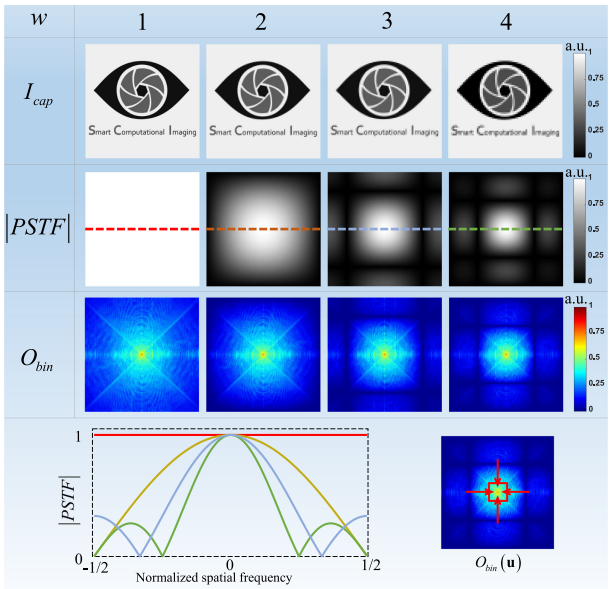

Fig. 8. The simulation results with the down-sampling factors $w = 1, 2, 3, 4$. The first row: the raw captured images; The second row: the corresponding pixel aliasing transfer functions; The third row: the Fourier spectrum of images with aliasing; The forth row: Left: the line profiles of the pixel aliasing transfer functions, Right: the sampling process with $w = 4$.

where $I(\mathbf{x})$ is the ideal image, $\mathbf{x} = (x, y)$ is two-dimensional coordinates on camera plane. S_a is a two-dimensional rectangular function which is defined to be 0 when $|x|$, $|y|$ is greater than $1/2\ w$, otherwise is defined to be $1/w^2$. Thus, in the frequency domain, this process can be represented as:

$$O_{bin}(\mathbf{u}) = \mathcal{F}\left(I_{bin}(\mathbf{x})\right) = O(\mathbf{u})\, PSTF(\mathbf{u}), \tag{15}$$

where $O_{bin}(\mathbf{u})$ and $O(\mathbf{u})$ is the Fourier transform of $I_{bin}(\mathbf{x})$ and $I(\mathbf{x})$, respectively. $PSTF(\mathbf{u})$ is the transfer function corresponding to the pixel binning, which takes the following form:

$$PSTF(\mathbf{u}) = PSTF(u_x, u_y) = sinc(wu_x) \cdot sinc(wu_y). \tag{16}$$

When $u_x = \pm\frac{r_x}{w}$ or $u_y = \pm\frac{r_y}{w}$ (r_x, r_y is a positive integer not greater than $w/2$ and the frequency has been normalized to $-1/2 \sim 1/2$.), $PSTF$ will be zero, suggesting that the corresponding spectral information is lost. Thus, the normalized first cut-off frequency will be $1/w$. Due to the previous assumptions that the ideal theoretical half-pitch resolution is $\Delta p/w$, the resolution limit after aliasing can be noted as:

$$q = \Delta p. \tag{17}$$

For the second step, the sampling process is that the ideal images are sampled at uniform intervals (w pixels). (see details in Appendix C when w is an integer.). The process shows that the high-frequency information will be mixed into the low-frequency region.

To show the information aliasing and spectrum loss resulting from the finite pixel size, the simulation results with the down-sampling factors $w = 1, 2, 3, 4$ are illustrated in Fig. 8. On the other hand, w can also be regarded as the resolution up-sampling factor for the pixel SR reconstruction algorithm from LR intensity measurements. The line curves of $PSTF(\mathbf{u})$ show that when w gradually increases, the more criss-crossed frequency gaps will appear, suggesting that the information around these frequencies will be exceptionally difficult to be recovered. When $w = 2$, $PSTF(\mathbf{u})$ tends to zero only at the highest frequency (the periphery of the Fourier spectrum). When $w > 2$, more spectral information at interlaced regions in $PSTF(\mathbf{u})$ becomes zero. The lower right of Fig. 8 shows the Fourier spectrum $O_{bin}(\mathbf{u})$ after pixel binning with $w = 4$, and the red rectangular area ($\frac{M}{w} \times \frac{N}{w}$) has the same dimensional size with the captured image. The whole process shows that the high-frequency information will be mixed into the low-frequency region within the red rectangle, and the aliasing problem will be more serious when w getting larger. For normal pixel size of the current image sensor (typically $0.8 - 5\ \mu$m), the pixel aliasing is a key limiting factor directly affecting the imaging resolution of the LFOCDHM system. When the resolution of the object to be reconstructed (by pixel SR algorithms [18], [26], [45], [52]) is w times higher than that limited by the original pixel size, the number of the captured raw LR images (theoretical amount of information) will linearly increase with a factor of w^2 [53].

5) Influence of the Finite Extent of Reconstructed Sub-FOV on Imaging Resolution: As we mentioned in the introduction, one of the most important advantages of the LFOCDHM is the large effective numerical aperture over a very large FOV. However, in practice, due to the limited processing capability and memory of the computer, usually each raw image is divided into several subregions for the holographic reconstruction, and the reconstructed sub-images are then stitched together to obtain the whole-FOV image. Owing to the limited extent of the selected reconstructed area (assuming that the shortest side length of the sub-FOV is ΔL), some high-angle diffraction patterns corresponding to the high-frequency of the object will not be included in the reconstructed area, leading to the reduction of imaging resolution. We attribute the effect of finite extent of reconstructed sub-FOV on the Fourier spectrum to the transfer function $RRTF$, where the lateral resolution limit in different directions are considered comprehensively, and finally ΔL is the key factor of the reconstructed resolution. The cut-off frequency of $RRTF$ is $|\mathbf{u}| = \frac{\Delta L/2}{\lambda\sqrt{{z_2}^2 + (\Delta L/2)^2}}$, which can also be deduced by the effective NA of the LFOCDHM system (as shown in Fig. 1), and the restricted half-pitch resolution is

$$q = \frac{1}{2\,|\mathbf{u}|} = \frac{\lambda\sqrt{4z_2^2 + \Delta L^2}}{2\Delta L}. \tag{18}$$

According to Eq. (18), in order to achieve the half-pitch resolution q, the side length of reconstructed sub-FOV should meet the following requirement:

$$\Delta L \geqslant \frac{2z_2\lambda}{\sqrt{4q^2 - \lambda^2}}. \tag{19}$$

In the simulation, we use $\lambda = 600$ nm, $z_2 = 200\ \mu$m, $\Delta p = 1\ \mu$m, and the theoretical half-pitch resolution $q = 1, 2, 4\ \mu$m can be calculated to verify the influence of the reconstructed area on the resolution. In Fig. 9, we can find that when the side length is $\Delta L_1 = 126\ \mu$m, the maximum half-pitch resolution is about $1\ \mu$m. However, when ΔL is getting smaller, the maximum half-pitch resolution will gradually decrease, e.g., when the side

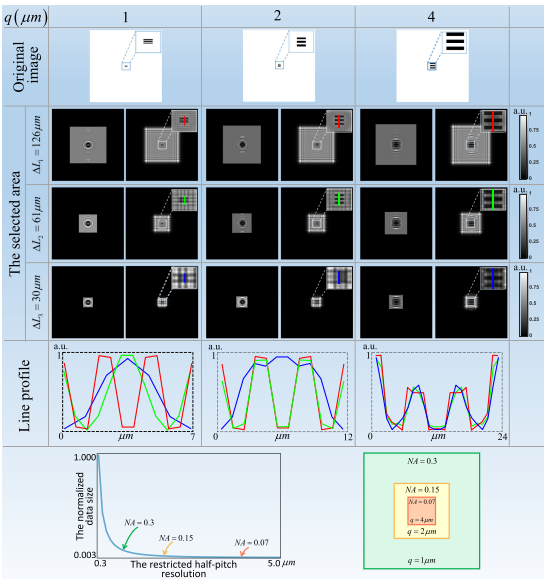

Fig. 9. From the first to fifth row: The simulation results with different reconstructed area sizes ($\Delta L_1 = 126\ \mu$m, $\Delta L_2 = 61\mu$m, $\Delta L_3 = 30\ \mu$m). The last row: Left: The half-pitch-resolution-dependent curve of the reconstructed area size; Right: The relative size of the reconstructed region corresponding to different half-pitch resolution.

length is $\Delta L_2 = 61\ \mu$m, the half-pitch resolution will reduce to 2μm. As shown in Fig. 9, the reconstructed area size almost increases exponentially with the improvement of the half-pitch resolution. Thus, for example, when the sample-to-sensor distance is 400 μm, in order to achieve the high imaging resolution close to the diffraction limit (e.g. NA ~ 0.8), the slide length of the reconstructed sub-FOV should be at least 2845 μm, which again brings a big challenge to the computational efficiency and memory requirement (especially when the pixel SR algorithm is used).

Furthermore, for each reconstruction of sub-FOV, only very limited central region can achieve the expected resolution. For the rest part, the region closer to the border will have lower imaging resolution. Thus, to decrease the influence of the finite extent of reconstructed sub-FOV on imaging resolution, in actual experiments, the selection of the reconstructed area faces a fundamental tradeoff between the loss of the high-frequency diffraction and the practicability of the implementation of the reconstruction algorithm. Moreover, in numerical calculation, the high-frequency scattered light diffracted from a point outside the selected region will have an impact on the background of reconstructions, e.g., additional twin image resulting from Fourier expansion at image boundary. Fortunately, the reconstructed resolution on the focus plane usually is rarely affected. It should be also noted that when pixel SR algorithm is used to achieve an expected sub-pixel resolution, the reconstructed area should be larger than theoretical one calculated by Eq. (19) to guarantee that such a resolution is theoretically achievable.

6) Comprehensive Influence of Multiple Factors on Imaging Resolution: Based on the above-mentioned analysis, the comprehensive absorption and phase transfer functions of all above-mentioned factors can be denoted as $ATF(\mathbf{u}) = ATFP \cdot TCTF \cdot SCTF \cdot PSTF \cdot RRTF$ and $PTF(\mathbf{u}) = PTFP \cdot TCTF \cdot SCTF \cdot PSTF \cdot RRTF$. Although the frequency response of each transfer function may slightly overshoot for the frequencies exceeds each first cut-off frequency, their contribution to imaging resolution can be neglected because the final imaging resolution is codetermined by multiple parameters, and the overall response value for these high frequencies in $ATF(\mathbf{u})$ and $PTF(\mathbf{u})$ after multiplication of each transfer functions will be quite small. Therefore, the final imaging resolution limit is determined by the minimum first cut-off frequencies of these sub-transfer functions. For a given LFOCDHM system where all system parameters are determined, we can calculate the resolution limit governed by each transfer function, Eqs. ((10), (13), (17), (18)), and then compare them with ideal coherent diffraction limit $\lambda/2$ to choose the maximal one as the ultimate theoretical imaging resolution. Note that the pixel SR methods are not considered in the above analysis. When the SR methods are considered, the theoretical limit resolution will be determined by the maximal value among Eqs. ((10), (13), (18)), the effective pixel size $\Delta p/w$, and $\lambda/2$. In this work, we only consider the cases when no pixel SR methods are employed. The results can be easily extended to the cases when pixel SR methods are involved.

For example, considering the situation in the experiments, the sample-to-senor distance is usually 450 μm, and the source-to-sample distance is about 10 cm. In addition, the illumination source has central wavelength 600 nm with the spectral width 10 nm and the luminous area of $100^2\pi\ \mu$m^2, and the sensor has the pixel size of 1.67 μm and imaging area of $6466 \times 4615\ \mu$m^2. According to Eqs. ((10), (13), (17),(18)), we can find that when no pixel SR methods are employed, the final resolution will be limited by the pixel size. The reconstructed results will be constrained principally by the spectral width $\Delta\lambda$ when the pixel SR methods are adopted. Thus, in a conventional experimental system, the pixel size is the key limiting factor for the high-resolution object reconstruction, but the developed pixel SR methods can effectively solve this spatial resolution reduction problem. In addition, the spectral width of the source is usually another main limiting factor for the resolution improvement, which is difficult to be solved or alleviated only with the numerical methods.

7) Optimization of the Imaging Resolution for a LFOCDHM System: Our theoretical models can be utilized to optimize the optical design for improving the imaging resolution when designing a LFOCDHM system. It is recommended that the following procedure should be adopted. (The minimum requirements of these parameters can be deduced by Eqs. ((10), (13), (18)) based on the resolution to be reconstructed.)

During the system construction stage:

1) Choose the light source with the best possible temporal and spatial coherence;

2) For low temporal coherent source such as LED, a narrow band-pass filter can be used to increase the temporal coherence of the source;

3) For low spatial coherent source with a large light-emitting area, a small pin-hole can be inserted in front of the source to increase the spatial coherence of the source;

4) Use an imaging sensor with the smallest possible pixel size to reduce aliasing.

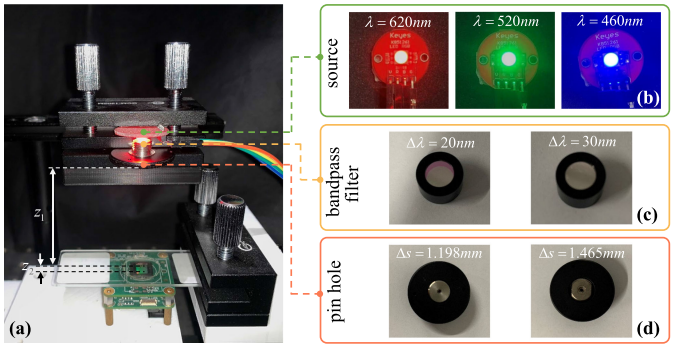

Fig. 10. (a) The photography of the LFOCDHM system. (b) Three central wavelengths of a light-emitting diode (LED). (c) Two narrow bandpass filters with spectral width $\Delta\lambda = 20$ nm and $\Delta\lambda = 30$ nm. (d) Two pin-holes with aperture size $\Delta s = 1.198$ mm and $\Delta s = 1.465$ mm.

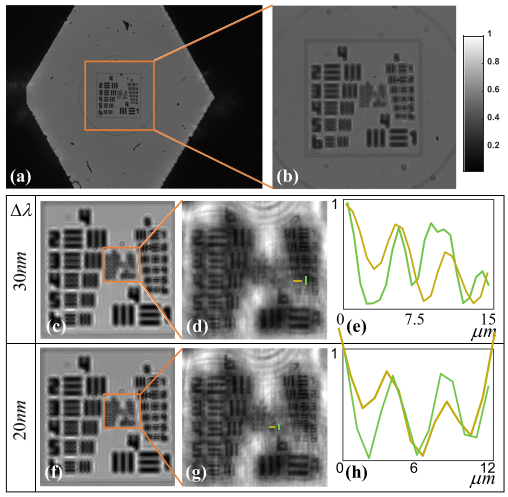

Fig. 11. The effect of temporal coherence on the spatial resolution. (a) the directly captured image, (b) the region to be reconstructed, the directly reconstructed results with the spectral width $\Delta\lambda = 30$ nm (c)-(e) and $\Delta\lambda = 20$ nm (f-h). The experimental condition: $\lambda = 520$ nm, $z_1 = 10$ cm, $z_2 = 1499$ μm.

During the data acquisition stage:

1) Minimize the sample-to-sensor distance z_2 to reduce the influence of temporal coherence of the source;

2) Maximum the ratio between source-to-sample distance z_1 and sample-to-sensor distance z_2 to reduce the influence of spatial coherence of the source;

3) Minimize the sample-to-sensor distance z_2 to reduce the influence of the finite extent of reconstructed sub-FOV;

4) For imaging phase object, use the multi-height phase retrieval algorithm with large sample-to-sensor distances z_2 to guarantee reliably phase recovery, especially for low-frequency components.

It should be emphasized that z_1 can only affect the spatial coherence, while z_2 can affect the selection of the size of the reconstructed region, the temporal and spatial coherence.

During the data processing stage:

1) Choose the largest possible reconstructed sub-FOV to reduce the influence of the finite extent of reconstructed sub-FOV.

2) Choose the proper position of the reconstructed sub-FOV to locate the targeted object in the center.

III. Experiments

A. Experimental Setup

Fig. 10(a) shows the fundamental experimental system structure. A broadband source (K851261, Keyes, China) providing the different central wavelengths [Fig. 10(b)], illuminates a sample that is mounted on a slide holder, and a CMOS image sensor chip (DMM 27UJ003-ML, the imaging source, Germany) is placed below the sample. To quantify the effect of the above-mentioned factors on the reconstruction results, we will respectively change the temporal [Fig. 10(c)], spatial [Fig. 10(d)] coherence of the light source, the pixel size of the imaging sensor, and the reconstructed region.

B. Influence of Temporal Coherence on Imaging Resolution

To quantify the spatial resolution alternation due to the above-mentioned factors respectively, we firstly change the temporal coherence of the light source by introducing different optical band-pass filters (spectral bandwidths $\Delta\lambda = 20, 30$ nm) into the experimental system. The partially coherent illumination is provided through a light-emitting diode (LED) which is placed far away ($z_1 \gg 20$ cm) from the sample plane to eliminate the effect of the spatial coherence. Fig. 11(a) shows the raw image directly captured by the camera, and Fig. 11(b) is the reconstructed region which is large enough to avoid its effect on the spatial resolution. The central wavelength of the illumination source is $\sim$520 nm, and the resolution target is $\sim$1499 μm (z_2) away from the sensor. When the spectral width is 30 nm, the reconstruction resolution is about 2.461 μm (5th element in group 7), and the theoretical reconstructed resolution is around 2.371 μm which lies between the 5th element and 6th element in group 7. When we reduce the spectral width to 20 nm, the theoretical half-pitch resolution calculated according to Eq. (10) is 1.936 μm, and the actual reconstruction resolution is $\sim$1.953 μm, as shown in Figs. 11(f)-(h) which corresponds to the 1st element in group 8 of the resolution target. Thus, the reconstructed results match well with the theoretical value calculated by Eq. (10). Note that in our experiment, we directly back propagate the image from the sensor plane to the object plane with the angular spectrum method [48], and no phase retrieval procedure is used to eliminate the twin-image artifacts in the background of the reconstructed images.

C. Influence of Spatial Coherence on Imaging Resolution

Next, we change the spatial coherence of the source by inserting different pin-holes (the diameter of the pin-holes $\Delta s = 1.198, 1.465$ mm) to verify the correctness of Eq. (13). The luminous area of a LED is usually in the ten thousands of square microns order of magnitude, thus, in order to show the influence of spatial coherence on resolution more intuitively, a diffuser is placed between the source and pin-hole to ensure that the luminous area equals the size of the pin hole. The center wavelength

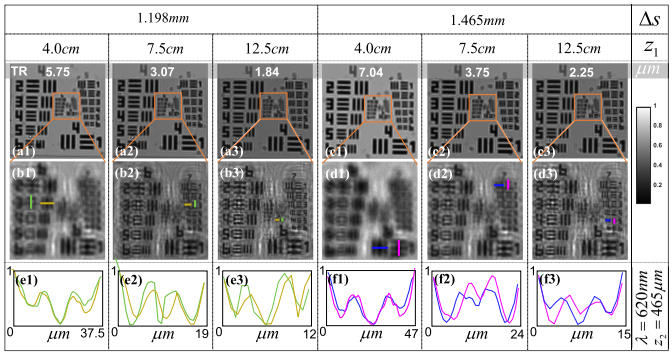

Fig. 12. The effect of spatial coherence on the spatial resolution. 'TR' is the abbreviation of theoretical resolution. (a1-b3) The reconstructed results with $\Delta s = 1.198$ mm. (c1)-(d3) The reconstructed results with $\Delta s = 1.465$ mm. (e1)-(f3) The line profiles of the corresponding marks in (b1)-(b3), (d1–d3).

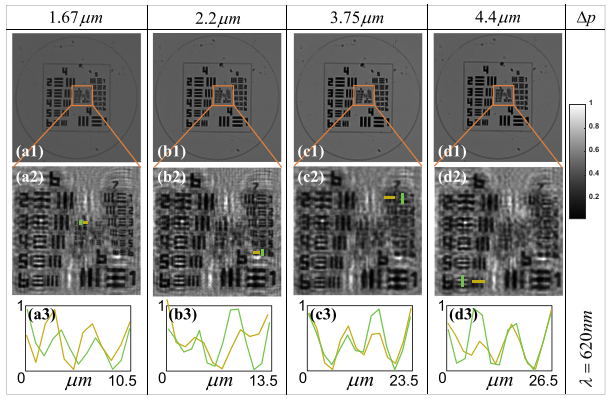

Fig. 13. The effect of pixel size on the spatial resolution. The directly reconstructed results with different pixel sizes 1.67 μm (a1)-(a3), 2.2 μm (b1)-(b3), 3.75 μm (c1)-(c3), 4.4 μm (d1)-(d3).

λ is $\sim$620 nm ($\Delta\lambda = 15$ nm) and the sample-to-sensor distance is $z_2 = 465$ μm. Fig. 12 shows the reconstruction results which are recovered by back-propagating the captured image to the object plane with angular spectrum method [48]. When $\Delta s = 1.198$ mm, the reconstructed results with the different source-to-sample distances z_1 are shown in Figs. 12(b1-b3). When z_1 is 4 cm, the theoretical half-pitch resolution is 5.75 μm, and the actual reconstructed result is $\sim$6.20 μm, corresponding to the 3rd element of group 6. Since the 4th element in group 6 corresponds to the half-pitch resolution of 5.52 μm, it can hardly be distinguished, as shown in Fig. 12(b1). In addition, when $\Delta s = 1.465$ mm, the experimental results also agree well with the theoretical values, as shown in Figs. 12(d1)-(d3). The line profiles along different resolution elements are respectively illustrated in Figs. 12(f1)-(f3). On the other hand, when z_1 is fixed, smaller Δs provides higher resolution. Thus, in the actual experiments, we can simply increase the source-to-sample distance z_1 to reduce the influence of spatial coherence, which is equivalent to reducing Δs.

D. Influence of Pixel Size on Imaging Resolution

In actual experiments, the pixel size of the image sensor is a key factor directly limiting the achievable spatial resolution. Although increasing the pixel resolution and reducing the pixel size has already become the major trend in consumer electronics, the minimum pixel size of the commercially available imaging sensor is around 0.8 μm, which is much larger than the coherent diffraction resolution limit. In order to give an intuitive comparison of the influence of pixel size on imaging resolution, we use the cameras with different pixel sizes (1.67 μm, 2.2 μm, 3.75 μm, 4.4 μm) to record the diffraction patterns. Figs. 13(a1)-(d1) show the reconstructed regions, and the reconstructed results are illustrated in Figs. 13(a2)-(d2). The wavelength of the source used in the system is 620 nm ($\Delta\lambda = 15$ nm) while the source-to-sample distance z_1 is large enough ($z_1 \gg 20$ cm) to exclude the influence of spatial coherence, and the sample-to-sensor distance z_2 is 465 μm. The line profiles corresponding to the smallest resolvable elements are shown in Figs. 13(a3)-(d3), suggesting that the experimental results are in agreement with the theoretical values limited by pixel sizes.

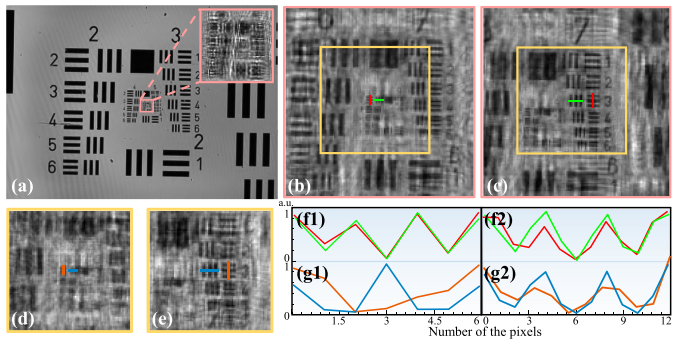

Fig. 14. The effect of the reconstructed region on spatial resolution. (a) is the raw image and the reconstructed region size of (b)-(c) corresponds to the pink square area in (a). (d)-(e) is the directly reconstructed results with the different selected areas separately corresponding to the yellow square area in (b)-(c). (f1)-(f2), (g1)-(g2) are the line profiles separately corresponding to (b)-(c), (d)-(e).

E. Influence of the Reconstructed Region on Imaging Resolution

In this experiment, the center wavelength of the light source λ is 620 nm ($\Delta\lambda = 15$ nm), and the sample-to-sensor distance z_2 is 547μm. According to Eq. (18), the size of the selected area for the reconstruction will affect the final imaging resolution. Fig. 14(a) gives the whole captured image, and the pink square area (198 μm wide) was extracted for the holographic reconstruction. The result is shown in Fig. 14(b), and corresponding line profiles are shown in Fig. 14(f1), suggesting that the resolution is at least 1.74 μm. When we select another region nearby with the same size, we can obtain the reconstruction result shown Fig. 14(c). If we reduce the size of the reconstructed region to the yellow boxed area (110 μm wide) in Figs. 14(b)-(c), the results shown in Figs. 14(d)-(e) indicate that the reconstructed resolution will decrease significantly. The line profiles in Figs. 14(g1)-(g2) manifest that the resolution is

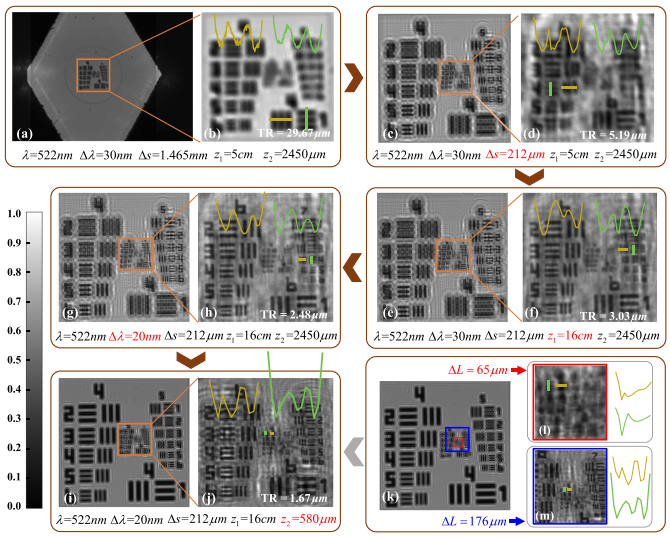

Fig. 15. The process of system optimization. (a-k) are the results of reconstruction under different conditions (on the top of each subgraphs) with pixel size 1.67 μm and the length of the reconstructed region 1080 μm. (l-m) The comparison between the results with different reconstructed regions.'TR' is the abbreviation of theoretical resolution.

reduced to only 3.10 μm (3 rd element in group 7), which is again in accordance with the theoretical prediction.

In addition to the size of reconstructed sub-FOV, the location of the object to be measured in the selected reconstructed sub-FOV will also affect the reconstructed resolution. As shown in Figs. 14(b)-(c), we can find that the 2nd element in group 8 can be distinguishable in Fig. 14(b) but not in Fig. 14(c). Thus, in order to ensure the expected high reconstruction resolution, the reconstructed sub-FOV should not be too small and the objects to be reconstructed are supposed to be located in the limited central region for each reconstructed sub-FOV. Meanwhile, the object-to-sensor distance z_2 should not be too large according to Eq. (18). Otherwise, the reconstructed region needs to be expanded accordingly to ensure the reconstruction resolution, which may significantly prolong the processing time and create difficulties in practical implementation of the reconstruction algorithm.

F. Example of the Multiple Optimized Design for the System

In the actual experiments, multiple factors will result in the resolution reduction of the imaging system. According to the conclusion of the resolution analysis, the system parameters are adjusted under limited conditions and optimized to improve the reconstructed resolution. For a preliminary LFOCDHM system, the center wavelength λ and the spectral bandwidth $\Delta\lambda$ of the LED are 522 nm and 30 nm respectively, and the diameter of the luminous area of the source is 1.465 mm. In addition, samples are placed randomly over the sensor at approximately a distance of 2450 μm. The pixel size of the camera is 1.67 mm and the results in Figs. 15(a)-(j) are reconstructed with a square region (1080 μm wide). According to Eqs. ((10), (13), (17), (18)), the theoretical resolution will be mainly limited by the spatial coherence which is 29.67 μm corresponding to 1st element in group 4 as shown in Figs. 15(a), (b). Thus, firstly reducing the luminous area (here the shape of the source is a square with the side length of 212 μm) to improve the spatial coherence, the theoretical resolution will be improved to 5.19 μm as shown in Figs. 15(c), (d) according to Eq. (24). In practical experiments, when Δs is difficult to be further reduced, based on Eq. (13), we can increase the z_1 to improve the spatial coherence. In theory, the resolution should be increased to 1.56 μm, but Figs. 15(e), (f) show that the reconstructed resolution is about 3.10 μm. From the comprehensive analysis, we can find that the resolution is limited by temporal coherence which should be 3.03 μm under the given conditions. Therefore, to improve the resolution, it is necessary to improve the temporal coherence of the whole system. A band-pass filter (20 nm) should be inserted into the system, and the slight increase in resolution can be seen in Figs. 15(g), (h). Sometimes, the temporal coherence of the light source is difficult to be improved, and so we can consider reducing z_2 which can improve temporal and spatial coherence of the LFOCDHM system at the same time based on Eqs. ((10), (13)) as shown in Figs. 15(i), (j). Fig. 15(j) shows that the resolution is limited by the pixel size, which means a camera with smaller pixel size or a SR algorithm with multi-frame acquisition is needed for further enhancing the imaging resolution. Fig. 15(l) shows that when the length of the reconstructed region (ΔL) is 65 μm, all elements in group 8 are indistinct, yet the 2nd elements in group 8 should be distinguished in theory with the same system parameters in Fig. 15(i), (j). When ΔL is increased to 176 μm, the 2nd elements in group 8 can be differentiated as shown in Fig. 15(m), and so ΔL must be larger than 176 μm for achieving the expected highest resolution.

Consequently, in practical experiments, we can roughly estimate the reconstructed resolution and the corresponding limiting factor based on the resolution analysis. Then the parameters are adjusted reasonably to obtain the optimal resolution under the given hardware conditions.

IV. Conclusion

In this work, we have conducted a systematical research on the effect of five major factors on imaging resolution of a LFOCDHM system, i.e., the sample-to-sensor distance, spatial and temporal coherence of the illumination, finite size of the equally spaced sensor pixels, and finite extent of the image sub-FOV used for the reconstruction. From the above analysis and experiments, it can be deduced that the most limiting factor restricting the imaging resolution of LFOCDHM is the sensor pixel size because the side-effect arising from other experimental factors is relatively easy to handle. For example, using a laser as an ideal temporally coherent light source, increasing source-to-sample distance to obtain the spatially quasi-coherent source. To reduce the effective size of the imaging sensor, pixel SR algorithms should be used. But even so, using an imaging sensor with smaller pixel size can still improve the quality of the SR reconstructions. Specifically, assuming that the expected resolution to be reconstructed is around 1 μm, and the up-sampling factor w will be different for various pixel sizes. When the pixel size is much closer to the desired resolution, the w will be smaller, so less information for the reconstruction is

required. When a higher up-sampling factor w is required (for large pixel size), more criss-crossed frequency gaps will appear, which can never be recovered even pixel SR reconstruction algorithms are used. Thus, for LFOCDHM techniques, a smaller pixel size is very helpfully to achieve higher resolution and need less information to reach the expected super-resolved resolution. On the other hand, using LED as the light source can make the system more compact, portable, low-cost. But the coherence length of the LED will also affect the reconstructed resolution. According to Eqs. ((10), (13)), increasing z_1 and decreasing z_2 can effectively improve the coherence of the LFOCDHM and improve the imaging resolution. Furthermore, decreasing z_2 can reduce the reconstructed area according to Eq. (19) when the desired resolution is determined.

The analysis of these parameters based on transfer functions has given the quantitative resolution limit determined by the minimum first cut-off frequency of these transfer functions. According to the quantitative relationship, the preliminary estimates of the ultimate resolution are available after employing the SR methods. Thus, the derived theoretical models can provide useful guidance for choosing the appropriate system parameters to obtain higher imaging resolution. To verify the validity of each theoretical model, we have used the variable-controlling method and only changed only one or two parameters during each experiment. The resolution target has been used to quantify the imaging resolution. The experimental results have confirmed the validity of our theoretical models.

Finally, it should be mentioned that, although in this work we have demonstrated how our theoretical models can be utilized to improve the imaging resolution by optimizing the optical design of a LFOCDHM system, it is possible to counteract the effects of these imperfect system parameters through certain computational approaches. For example, for the poor spatial coherence, the low-resolution effects can be eliminated by measuring the point spread function of the source and then performing deconvolution. When the pixel size is unsatisfactory, sub-pixel lateral shifts combining with calculating the cross correlation between the adjacent images by means of a fast Fourier transform (FFT) and then locating its peak, can generate the SR reconstructions. Based on the transfer functions we have derived, we can easily establish the forward image formation model (from object to image) for a given LFOCDHM system. Then certain mathematical algorithm should be adopted to recover the ideal object information from the actual measurement, i.e., to solve the corresponding inverse problem. In future work, we will make efforts to address the resolution reduction associated with these factors and compensate for their adverse impact through post-processing algorithms.

APPENDIX

A. The Weak Phase Object Approximation

The complex transmittance of a weak object can be represented as

$$t(\mathbf{x}) = a(\mathbf{x})\, e^{i\phi(\mathbf{x})} \underset{a(\mathbf{x})=a_0+\Delta a(\mathbf{x})}{\approx} a(\mathbf{x})\left[1+i\phi(\mathbf{x})\right] \approx a_0 + \Delta a(\mathbf{x}) + i a_0 \phi(\mathbf{x}), \tag{20}$$

where $a(\mathbf{x})$ is the absorption distribution with a mean value of a_0, $\phi(\mathbf{x})$ is the phase distribution, $\mathbf{x}$ represents the two-dimensional coordinate (x,y) in spatial domain. Taking Fourier transform of both sides of Eq. (20), the Fourier spectrum of $t(\mathbf{x})$ can be obtained as

$$T(\mathbf{u}) = a_0 \delta(\mathbf{u}) + A(\mathbf{u}) + i a_0 \Phi(\mathbf{u}), \tag{21}$$

where $\mathbf{u}$ is the two-dimensional coordinate in frequency domain, $\delta(\mathbf{u})$ is the Dirac Delta function, $A(\mathbf{u})$ and $\Phi(\mathbf{u})$ respectively represent the Fourier spectrum of the absorption and phase distribution. Thus, the spectrum of the complex wave-front on the camera plane can be denoted as:

$$W_{cam}(\mathbf{u}) = T(\mathbf{u})\, P(\mathbf{u}) = a_0 \delta(\mathbf{u})\, P(\mathbf{u}) + A(\mathbf{u})\, P(\mathbf{u}) + i a_0 \Phi(\mathbf{u})\, P(\mathbf{u}), \tag{22}$$

where $P(\mathbf{u}) = e^{ikz_2\sqrt{1-\lambda^2|\mathbf{u}|^2}}$ represents the defocus pupil function.

B. The Resolution Derivation When the Shape of the Source is a Rectangle

Although most of the time the lighting source is circular, sometimes it also can be rectangular, especially for the LED source. According to Eq. (11) , assuming that the illumination source is a square with a width of Δs, the spatial coherence transfer function ($SCTF$) can be expressed as:

$$SCTF(\mathbf{u}) = \mathcal{F}(PSF) = \frac{\sin\left(\pi \frac{z_2 \Delta s}{z_1}|\mathbf{u}|\right)}{\pi \frac{z_2 \Delta s}{z_1}|\mathbf{u}|} = sinc\left(\frac{z_2 \Delta s}{z_1}|\mathbf{u}|\right). \tag{23}$$

Based on Eq. (23), we can derive that the first cut-off frequency is $|\mathbf{u}| = \frac{z_1}{z_2 \Delta s}$, and the corresponding reconstructed half-pitch resolution is

$$q = \frac{1}{2|\mathbf{u}|} = \frac{z_2 \Delta s}{2 z_1}. \tag{24}$$

C. The Sampling Process

One way to model sampling is to multiply $I(\mathbf{x})$ by a sampling function $S_w(\mathbf{x})$ equal to a train of impulses w units apart [54]. That is

$$I_{Sam}(\mathbf{x}) = I_{ali}(\mathbf{x}) \cdot S_w(\mathbf{x}), \tag{25}$$

where $I_{Sam}(\mathbf{x})$ is the image after sampling, $S_w(\mathbf{x})$ is the two-dimensional comb function. Here $S_w(\mathbf{x}) = S_w(x,y) = \sum_{\alpha=-M/2}^{M/2-1} \sum_{\beta=-N/2}^{N/2} \delta(x-\alpha w, y-\beta w)$. In the Fourier space, Eq. (25) can be written as:

$$O_{Sam}(\mathbf{u}) = O_{ali}(\mathbf{u}) * \tilde{S}_w(\mathbf{u}), \tag{26}$$

where $\tilde{S}_w(\mathbf{u}) = \sum_{\alpha=0}^{w-1} \sum_{\beta=0}^{w-1} \delta(u_x - \alpha \frac{M}{w}, u_y - \beta \frac{N}{w})$. In discrete numerical calculation, the dimension of the captured image is different from that of the original image, so the sampling process (including the selection of the central low-frequency part in the frequency domain) also can be written in the form of matrix:

$O_{cap} = M_{left} O_{ali} M_{right}$, where M_{left} is a $m \times M$ matrix, and M_{right} is a $n \times N$ matrix. Concretely, $M_{left} = [\overbrace{\mathbf{A} \cdots \mathbf{A}}^{w}]$, $\mathbf{A} = \begin{bmatrix} \mathbf{A_1} & \mathbf{A_2} \\ \mathbf{A_2} & \mathbf{A_1} \end{bmatrix}$. When $\mathbf{I}_A$ is the $\frac{M}{2w} \times \frac{M}{2w}$ unit matrix, then $\mathbf{A}_1$ and $\mathbf{A}_2$ can be denoted by $\mathbf{A}_1 = \frac{\mathrm{I}_A - (-1)^w \mathbf{I}_A}{2}$, $\mathbf{A}_2 = \frac{\mathrm{I}_A + (-1)^w \mathbf{I}_A}{2}$. Analogously, $M_{right} = [w\{\begin{matrix} \mathbf{B} \\ \vdots \\ \mathbf{B} \end{matrix}]$, $\mathbf{B} = \begin{bmatrix} \mathbf{B_1} & \mathbf{B_2} \\ \mathbf{B_2} & \mathbf{B_1} \end{bmatrix}$, $\mathbf{B}_1 = \frac{\mathrm{I}_B - (-1)^w \mathbf{I}_B}{2}$, $\mathbf{B}_2 = \frac{\mathrm{I}_B + (-1)^w \mathbf{I}_B}{2}$, where $\mathbf{I}_B$ is a $\frac{N}{2w} \times \frac{N}{2w}$ unit matrix.

ACKNOWLEDGMENT

The authors gratefully acknowledge financial support from China Scholarship Council.

REFERENCES

[1] H. R. Maricq and E. C. LeRoy, "Patterns of finger capillary abnormalities in connective tissue disease by "wide-field" microscopy," *Arthritis Rheumatism*, vol. 16, no. 5, pp. 619–628, 1973.

[2] A. Huisman, A. Looijen, S. M. V. D. Brink, and P. J. V. Diest, "Creation of a fully digital pathology slide archive by high-volume tissue slide scanning," *Human Pathol.*, vol. 41, no. 5, pp. 751–757, 2010.

[3] B. Ma *et al.*, "Use of autostitch for automatic stitching of microscope images," *Micron*, vol. 38, no. 5, pp. 492–499, 2007.

[4] V. Mico, Z. Zalevsky, P. García-Martínez, and J. García, "Synthetic aperture superresolution with multiple off-axis holograms," *J. Opt. Soc. Amer. A*, vol. 23, no. 12, pp. 3162–3170, 2006.

[5] C. Yuan, H. Zhai, and H. Liu, "Angular multiplexing in pulsed digital holography for aperture synthesis," *Opt. Lett.*, vol. 33, no. 20, pp. 2356–2358, 2008.

[6] T. R. Hillman, G. Thomas, S. A. Alexandrov, and D. D. Sampson, "High-resolution, wide-field object reconstruction with synthetic aperture fourier holographic optical microscopy," *Opt. Express*, vol. 17, no. 10, pp. 7873–7892, 2009.

[7] Y. Kim *et al.*, "Common-path diffraction optical tomography for investigation of three-dimensional structures and dynamics of biological cells," *Opt. Express*, vol. 22, no. 9, pp. 10 398–10 407, 2014.

[8] Y. Kim, H. Shim, K. Kim, H. Park, S. Jang, and Y. Park, "Profiling individual human red blood cells using common-path diffraction optical tomography," *Sci. Rep.*, vol. 4, 2014, Art. no. 6659.

[9] J. Lim *et al.*, "Comparative study of iterative reconstruction algorithms for missing cone problems in optical diffraction tomography," *Opt. Express*, vol. 23, no. 13, pp. 16 933–16 948, 2015.

[10] G. Zheng, R. Horstmeyer, and C. Yang, "Wide-field, high-resolution fourier ptychographic microscopy," *Nature Photon.*, vol. 7, no. 9, pp. 739–745, 2013.

[11] X. Ou, R. Horstmeyer, C. Yang, and G. Zheng, "Quantitative phase imaging via fourier ptychographic microscopy," *Opt. Lett.*, vol. 38, no. 22, pp. 4845–4848, 2013.

[12] L. Tian, X. Li, K. Ramchandran, and L. Waller, "Multiplexed coded illumination for fourier ptychography with an led array microscope," *Biomed. Opt. Express*, vol. 5, no. 7, pp. 2376–2389, 2014.

[13] X. Ou, R. Horstmeyer, G. Zheng, and C. Yang, "High numerical aperture fourier ptychography: principle, implementation and characterization," *Opt. Express*, vol. 23, no. 3, pp. 3472–3491, 2015.

[14] C. Zuo, J. Sun, and Q. Chen, "Adaptive step-size strategy for noise-robust fourier ptychographic microscopy," *Opt. Express*, vol. 24, no. 18, pp. 20 724–20 744, 2016.

[15] J. Sun, Q. Chen, Y. Zhang, and C. Zuo, "Efficient positional misalignment correction method for fourier ptychographic microscopy," *Biomed. Opt. Express*, vol. 7, no. 4, pp. 1336–1350, 2016.

[16] J. Sun, Q. Chen, Y. Zhang, and C. Zuo, "Sampling criteria for fourier ptychographic microscopy in object space and frequency space," *Opt. Express*, vol. 24, no. 14, pp. 15 765–15 781, 2016.

[17] G. Zheng, S. A. Lee, Y. Antebi, M. B. Elowitz, and C. Yang, "The epetri dish, an on-chip cell imaging platform based on subpixel perspective sweeping microscopy (spsm)," *Proc. Nat. Acad. Sci.*, vol. 108, no. 41, pp. 16 889–16 894, 2011.

[18] W. Luo, Y. Zhang, Z. Göröcs, A. Feizi, and A. Ozcan, "Propagation phasor approach for holographic image reconstruction," *Sci. Rep.*, vol. 6, 2016, Art. no. 22738.

[19] Y. Rivenson *et al.*, "Deep learning enhanced mobile-phone microscopy," *ACS Photon.*, vol. 5, no. 6, pp. 2354–2364, 2018.

[20] J. Zhang, Q. Chen, J. Li, J. Sun, and C. Zuo, "Lensfree dynamic super-resolved phase imaging based on active micro-scanning," *Opt. Lett.*, vol. 43, no. 15, pp. 3714–3717, 2018.

[21] J. Garcia-Sucerquia, W. Xu, M. Jericho, and H. J. Kreuzer, "Immersion digital in-line holographic microscopy," *Opt. Lett.*, vol. 31, no. 9, pp. 1211–1213, 2006.

[22] A. Ozcan and E. McLeod, "Lensless imaging and sensing," *Annu. Rev. Biomed. Eng.*, vol. 18, pp. 77–102, 2016.

[23] O. Mudanyali *et al.*, "Compact, light-weight and cost-effective microscope based on lensless incoherent holography for telemedicine applications," *Lab a Chip*, vol. 10, no. 11, pp. 1417–1428, 2010.

[24] T.-W. Su, A. Erlinger, D. Tseng, and A. Ozcan, "Compact and light-weight automated semen analysis platform using lensfree on-chip microscopy," *Analytical Chemistry*, vol. 82, no. 19, pp. 8307–8312, 2010.

[25] X. Cui *et al.*, "Lensless high-resolution on-chip optofluidic microscopes for caenorhabditis elegans and cell imaging," *Proc. Nat. Acad. Sci.*, vol. 105, no. 31, pp. 10 670–10 675, 2008.

[26] W. Bishara *et al.*, "Holographic pixel super-resolution in portable lensless on-chip microscopy using a fiber-optic array," *Lab a Chip*, vol. 11, no. 7, pp. 1276–1279, 2011.

[27] A. Greenbaum *et al.*, "Imaging without lenses: achievements and remaining challenges of wide-field on-chip microscopy," *Nature Methods*, vol. 9, no. 9, pp. 889–895, 2012.

[28] J. Barton, "Removing multiple scattering and twin images from holographic images," *Phys. Rev. Lett.*, vol. 67, no. 22, p. 3106, 1991.

[29] T. Latychevskaia and H.-W. Fink, "Solution to the twin image problem in holography," *Phys. Rev. Lett.*, vol. 98, no. 23, 2007, Art. no. 233901.

[30] S. C. Park, M. K. Park, and M. G. Kang, "Super-resolution image reconstruction: a technical overview," *IEEE Signal Process. Mag.*, vol. 20, no. 3, pp. 21–36, May 2003.

[31] J. Zhang, J. Sun, Q. Chen, J. Li, and C. Zuo, "Adaptive pixel-super-resolved lensfree in-line digital holography for wide-field on-chip microscopy," *Sci. Rep.*, vol. 7, no. 1, 2017, Art. no. 11777.

[32] Y. Hao and A. Asundi, "Resolution analysis of a digital holography system," *Appl. Opt.*, vol. 50, no. 2, pp. 183–193, 2011.

[33] G. B. Parrent and G. O. Reynolds, "Resolution limitations of lensless photography," *Opt. Eng.*, vol. 3, no. 6, 1965, Art. no. 306219.

[34] T. E. Agbana, H. Gong, A. S. Amoah, V. Bezzubik, M. Verhaegen, and G. Vdovin, "Aliasing, coherence, and resolution in a lensless holographic microscope," *Opt. Lett.*, vol. 42, no. 12, pp. 2271–2274, 2017.

[35] L. Xu, X. Peng, Z. Guo, J. Miao, and A. Asundi, "Imaging analysis of digital holography," *Opt. Express*, vol. 13, no. 7, pp. 2444–2452, 2005.

[36] D. P. Kelly, B. M. Hennelly, N. Pandey, T. J. Naughton, and W. T. Rhodes, "Resolution limits in practical digital holographic systems," *Opt. Eng.*, vol. 48, no. 9, 2009, Art. no. 095801.

[37] A. Doblas, E. Sánchez-Ortiga, M. Martínez-Corral, and J. Garcia-Sucerquia, "Study of spatial lateral resolution in off-axis digital holographic microscopy," *Opt. Commun.*, vol. 352, pp. 63–69, 2015.

[38] D. P. Kelly and D. Claus, "Filtering role of the sensor pixel in fourier and fresnel digital holography," *Appl. Opt.*, vol. 52, no. 1, pp. A336–A345, 2013.

[39] A. Ozcan and U. Demirci, "Ultra wide-field lens-free monitoring of cells on-chip," *Lab a Chip*, vol. 8, no. 1, pp. 98–106, 2008.

[40] W. Luo, Y. Zhang, A. Feizi, Z. Göröcs, and A. Ozcan, "Pixel super-resolution using wavelength scanning," *Light: Sci. Appl.*, vol. 5, no. 4, 2016, Art. no. e16060.

[41] D. Tseng *et al.*, "Lensfree microscopy on a cellphone," *Lab a Chip*, vol. 10, no. 14, pp. 1787–1792, 2010.

[42] S. V. Kesavan *et al.*, "High-throughput monitoring of major cell functions by means of lensfree video microscopy," *Sci. Rep.*, vol. 4, 2014, Art. no. 5942.

[43] S. K. Ludwig *et al.*, "Calling biomarkers in milk using a protein microarray on your smartphone," *PLoS One*, vol. 10, no. 8, 2015, Art. no. e0134360.

[44] Z. Xiong, J. E. Melzer, J. Garan, and E. McLeod, "Optimized sensing of sparse and small targets using lens-free holographic microscopy," *Opt. Express*, vol. 26, no. 20, pp. 25 676–25 692, 2018.

[45] W. Bishara, T.-W. Su, A. F. Coskun, and A. Ozcan, "Lensfree on-chip microscopy over a wide field-of-view using pixel super-resolution," *Opt. Express*, vol. 18, no. 11, pp. 11181–11191, 2010.
[46] E. J. Kirkland, *Advanced Computing in Electron Microscopy*. Berlin, Germany: Springer Science & Business Media, 2010.
[47] C. Zuo, J. Sun, J. Li, J. Zhang, A. Asundi, and Q. Chen, "High-resolution transport-of-intensity quantitative phase microscopy with annular illumination," *Scientific Rep.*, vol. 7, no. 1, 2017, Art. no. 7654.
[48] J. W. Goodman, *Introduction to Fourier Optics*. Greenwood, CO, US: Roberts and Company Publishers, 2005.
[49] D. Hamilton, C. Sheppard, and T. Wilson, "Improved imaging of phase gradients in scanning optical microscopy," *J. Microsc.*, vol. 135, no. 3, pp. 275–286, 1984.
[50] S. Feng and J. Wu, "Resolution enhancement method for lensless in-line holographic microscope with spatially-extended light source," *Opt. Express*, vol. 25, no. 20, 2017, Art. no. 24735.
[51] Z. Jingshan, L. Tian, J. Dauwels, and L. Waller, "Partially coherent phase imaging with simultaneous source recovery," *Biomed. Opt. Express*, vol. 6, no. 1, pp. 257–265, 2015.
[52] G. Zheng, S. A. Lee, S. Yang, and C. Yang, "Sub-pixel resolving optofluidic microscope for on-chip cell imaging," *Lab a Chip*, vol. 10, no. 22, pp. 3125–3129, 2010.
[53] J. Miao, D. Sayre, and H. Chapman, "Phase retrieval from the magnitude of the fourier transforms of nonperiodic objects," *J. Opt. Soc. Amer. A*, vol. 15, no. 6, pp. 1662–1669, 1998.
[54] R. C. Gonzalez and P. Wintz, *Digital Image Processing*, Berlin, Germany: Springer, 1977, no. 13.